PNAS RESEARCH ARTICLE | MICROBIOLOGY

Electrochemical cofactor recycling of bacterial microcompartments

Markus Sutter[a,b,c], Lisa M. Utschig[d], Jens Niklas[d], Sathi Paul[e], Darren N. Kahan[f], Sayan Gupta[c], Oleg G. Poluektov[d], Bryan H. Ferlez[a,1], Nicholas M. Tefft[g], Michaela A. TerAvest[g], David P. Hickey[h], Josh V. Vermaas[a,g], Corie Y. Ralston[c,e], and Cheryl A. Kerfeld[a,b,c,g,2]

Affiliations are included on p. 10.

Edited by Danielle Tullman-Ercek, Northwestern University, Evanston, IL; received July 16, 2024; accepted October 15, 2024 by Editorial Board Member Amy C. Rosenzweig

Bacterial microcompartments (BMCs) are prokaryotic organelles that consist of a protein shell which sequesters metabolic reactions in its interior. While most of the substrates and products are relatively small and can permeate the shell, many of the encapsulated enzymes require cofactors that must be regenerated inside. We have analyzed the occurrence of an enzyme previously assigned as a cobalamin (vitamin B_{12}) reductase and, curiously, found it in many unrelated BMC types that do not employ B_{12} cofactors. We propose Nicotinamide adenine dinucleotide (NAD+) regeneration as the function of this enzyme and name it Metabolosome Nicotinamide Adenine Dinucleotide Hydrogen (NADH) dehydrogenase (MNdh). Its partner shell protein BMC-T^{SE} (tandem domain BMC shell protein of the single layer type for electron transfer) assists in passing the generated electrons to the outside. We support this hypothesis with bioinformatic analysis, functional assays, Electron Paramagnetic Resonance spectroscopy, protein voltammetry, and structural modeling verified with X-ray footprinting. This finding represents a paradigm for the BMC field, identifying a new, widely occurring route for cofactor recycling and a new function for the shell as separating redox environments.

bacterial microcompartment | metabolosome | cofactor recycling

Significance

Bacterial microcompartments (BMCs) are organelles composed of protein that encapsulate specific metabolic processes and colocalize enzymes with their substrates and cofactors. Small pores in the shell proteins facilitate the exchange of substrates and products, but they are not large enough to allow efficient passage of larger molecules like cofactors. Here, we propose and characterize a method of cofactor regeneration that involves a transfer of electrons to the outside of the BMC. This finding represents a new paradigm for general BMC function, identifying a new route of cofactor recycling and a new function for the shell as separating redox environments; these findings have implications for both the native BMC systems as well for the engineering of BMCs with redox functionality.

Bacterial microcompartments (BMCs) are protein shells encapsulating enzymes that are found in a large variety of prokaryotes (1, 2). There are two distinct major classes, anabolic carboxysomes found mostly in cyanobacteria that fix carbon dioxide with encapsulated RuBisCO (3), and catabolic metabolosomes that process a variety of organic compounds (4, 5). The canonical reaction mechanism of metabolosomes starts with an encapsulated signature enzyme that generates an aldehyde that is then processed by an aldehyde dehydrogenase (AldDh) to a Coenzyme A adduct (Fig. 1*A*) (2, 4–6). The AldDh reaction involves a reduction of Nicotinamide adenine dinucleotide (NAD+) to Nicotinamide Adenine Dinucleotide Hydrogen (NADH), and the regeneration of NAD+ is thought to proceed through a side reaction that generates an alcohol from the aldehyde substrate (Fig. 1*A*) (7). The most well-known metabolosomes are the ethanolamine utilization (EUT) (8) and propanediol utilization (PDU) (9) (BMCs). More recently a number of additional metabolosome types have been characterized: Planctomycete and Verrucomicrobia (PVM) microcompartment (10), Glycyl radical microcompartments (GRMs) (11–14), aminoethane degrading (RMM: Rhodococcus and Mycobacteria microcompartment or AAUM: aminoethane utilizing microcompartment) (15), a taurine degrading (16, 17) and an aromatic substrate degrading BMC (ARO) (18).

Metabolosome BMCs are typically between 55 to 200 nm in diameter (9, 10) and their shells consist of proteins formed from two structural domains that are conserved across all BMCs. The BMC-H and BMC-T proteins contain the pfam00936 domain and form hexameric and trimeric hexagonal tiles, respectively. The hexagonal tiles have a central pore at the center of symmetry that is thought to be the main conduit into the shell for metabolites (19, 20); however, their typical diameter of around 5 Å makes them less suitable for larger molecules like cofactors. For the most common type of BMC-T, the BMC-T^{S}, which consist of a tandem fusion of two pfam00936 domains that do not further dimerize (hence superscript "S" for single), there are two main subtypes on a phylogenetic tree (1): 1) the carboxysome shell protein CcmO and 2), the proteins related to PduT, a BMC-T^{S} first characterized from the PDU BMC (21) which contains a 4Fe-4S cluster in its central pore [CP(G/S)K motif, C38 in *Salmonella enterica*]. The second structural domain necessary for the formation of BMC shells is the pfam03319 domain that forms the BMC-P pentamers that cap an overall icosahedral or polyhedral structure (22–26).

When examining model shells that contain representative shell protein components (23) it seems unlikely and inefficient that larger cofactors such as NADH or Coenzyme

Author contributions: M.S., L.M.U., B.H.F., M.A.T., J.V.V., C.Y.R., and C.A.K. designed research; M.S., L.M.U., J.N., S.P., D.N.K., S.G., O.G.P., B.H.F., N.M.T., M.A.T., D.P.H., and J.V.V. performed research; M.S., L.M.U., J.N., S.G., O.G.P., B.H.F., M.A.T., D.P.H., J.V.V., C.Y.R., and C.A.K. analyzed data; and M.S. and C.A.K. wrote the paper.

The authors declare no competing interest.

This article is a PNAS Direct Submission. D.T.-E. is a guest editor invited by the Editorial Board.

[1]Present address: Department of Molecular Biology and Genetics, Cornell University, Ithaca, NY 14583

[2]To whom correspondence may be addressed. Email: ckerfeld@lbl.gov.

This article contains supporting information online at https://www.pnas.org/lookup/suppl/doi:10.1073/pnas.2414220121/-/DCSupplemental.

Published November 25, 2024.

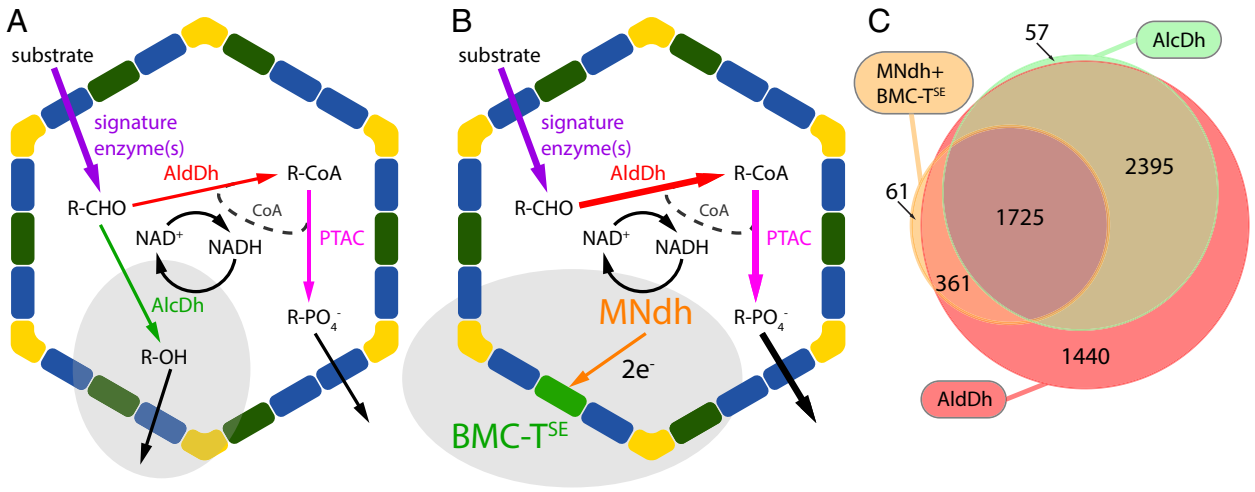

Fig. 1. Metabolosome reaction schemes and MNdh distribution. (*A*) Traditional metabolosome scheme. (*B*) MNdh NAD+ regeneration scheme. (*C*) Co-occurrence of NAD+ cofactor regeneration enzymes with AldDh in BMC loci shown as an Euler diagram (not visualized is an overlap of alcohol dehydrogenase (AlcDh) and MNdh/BMC-TSE and no AldDh with 25 occurrences). Abbreviations: AldDh: Aldehyde dehydrogenase; AlcDh: Alcohol dehydrogenase; PTAC: phosphotransacetylase; CoA: Coenzyme A.

A are exchanged across the shell for each turnover. Moreover, pores in the shell protein tiles are typically too small to permit passage of cofactor molecules. There are examples of gated pores of larger diameter shell proteins (BMC-T^D) (23, 27–29) that could conceivably conduct cofactors; however, these are not found in all shells, and are typically a minor fraction when present (30). Their role would be relatively low throughput and would require a concentration gradient to be established across the shell. Instead, it is more likely that cofactors are acquired during assembly [as in the case of the Coenzyme A associated with the phosphotransacylase PduL (31)] and regenerated by core metabolosome enzymes. As such they form a private cofactor pool for organelle function.

As part of a previous bioinformatics analysis (1) we surveyed the distribution of all enzymes within predicted BMC loci and noticed that the enzyme known as PduS is found frequently in loci other than the PDU; indeed it is distributed across many functionally diverse BMC types and species. The proposed function of this protein in literature is performing the reduction from aquacob(III)alamin to cob(I)alamin as part of the regeneration of inactivated adenosylcobalamin (32–34) in Vitamin B_{12}/cobalamin-dependent metabolosomes. This specialized function, however, is unlikely to be relevant in many of the non-PDU or EUT BMC types as there are no known BMC-related enzymes using B_{12} other than the PDU and EUT signature enzymes. Furthermore, we found that consistently encoded adjacent to it was a PduT homolog that contained the motif for Fe-S cluster binding. Here, we present a comprehensive bioinformatic analysis of this non-canonically occurring PduS/PduT pair, structural modeling, and functional and spectroscopic data to show that the PduS-like protein acts in conjunction with its cognate PduT-like protein to pass two electrons from the Flavin mononucleotide (FMN) cofactor via three 4Fe-4S clusters to an acceptor outside the shell, thereby regenerating NAD+ within the BMC. Accordingly, we propose a more universal name for PduS, MNdh, for metabolosome NADH dehydrogenase, and we rename its co-occurring PduT homolog BMC-T^{SE} (E for electron transfer) because it contains a central 4Fe-4S cluster. BMC-T^{SE} and MNdh likely form a cofactor regeneration system and the widespread occurrence of these two proteins across functionally diverse BMCs that highlights their potential importance. Knowledge of this housekeeping cofactor recycling module allows us to better understand the native metabolosome reaction mechanisms as well as enable the use of NAD recycling for engineered systems.

Results

Bioinformatics Analysis of the MNdh/BMC-T^{SE} Prevalence. We undertook a comprehensive survey for the presence of MNdh and for BMC-T^{SE} in all BMC loci, using the BMC locus dataset from Sutter et al. (1). MNdh can be found in 2,172 of over 7,000 BMC loci, across a large functional variety of metabolosomes (*SI Appendix*, Fig. S1 and Table S1). In 97% of the MNdh containing loci, the gene for BMC-T^{SE} is located immediately adjacent (and in 1.8% two genes away) (*Materials and Methods* and Dataset S1). In the primary structure of the BMC-T^S proteins encoded adjacent to the gene for MNdh, we observed a universal conservation of the CP(G/S)K Fe-S cluster binding motif. This is in contrast to BMC-T^S homologs not in proximity to MNdh; in these, the pore cysteine is not conserved [such as in the BMC-T^S of the structurally characterized *Haliangium ochraceum* BMC-T (35)].

However, in conflict with the originally proposed function of the MNdh for Vitamin B_{12}/cobalamin regeneration, many of the functionally varied BMC types are not predicted to utilize B_{12}. Among them are the more recently characterized GRM, PVM, and Taurine utilizing BMC (also known as GRMguf) (10, 12, 16, 17) as well as many BMC types with functions that have yet to be established (MIC, MUF, FRAG, SPU) (1, 4) (*SI Appendix*, Fig. S1 and Table S1). MNdh is only found in BMC types that also contain an AldDh that is essential for the BMC function for the established metabolosome types and likely also for the yet-to-be-characterized ones. This type of AldDh uses NAD+ as an electron acceptor, generating NADH. Typically, the NAD recycling is carried out by the coencapsulated alcohol dehydrogenase (Fig. 1*A*), but we noted a large number (361) of BMCs lacking a gene for the alcohol dehydrogenase, but containing PduS/T (Fig. 1*C*). This led us to formulate a hypothesis that the primary function of MNdh is to regenerate the NAD+ cofactor inside the BMC lumen (Fig. 1*B*), passing the electrons to the outside of the BMC via the Fe-S cluster of BMC-T^{SE}. An advantage of this type of regeneration vs. the traditional type of NAD+ regeneration with alcohol dehydrogenase is that it prevents the production of the alcohol side product. In this pathway, all of the input substrate is converted to the more valuable Coenzyme A-product (Fig. 1*B*).

The occurrence of MNdh in BMC functional types is variable, however many of them have a higher than 90% occurrence for a given type (*SI Appendix*, Fig. S1 and Table S1). Many of them co-occur with alcohol dehydrogenase that performs the canonical NAD+ regeneration (Fig. 1*C* and *SI Appendix*, Table S1), as in the case of the highly characterized PDU type BMC of *S. enterica* (9). Both the alcohol dehydrogenase and MNdh/BMC-T^{SE} almost exclusively co-occur with the AldDh, highlighting their functional dependence. The large number of loci (1,725, Fig. 1*C*) that contain both NAD+ regeneration systems is an indication of their functional importance in cofactor recycling. Potentially they can be either both active at the same time or active under different circumstances, such as variations in electron acceptor availability.

Additional evidence of a more general, "housekeeping" role in metabolosome function (as opposed to a substrate-specific role) for MNdh-BMC-T^{SE} emerges from consideration of their phylogeny and BMC type distribution. We generated a phylogenetic tree of MNdh sequences and analyzed their correlation with BMC type and phylogenetic origin (*SI Appendix*, Fig. S2). There is surprisingly little correlation between the BMC type and sequence of MNdh. For example, the MNdh found in the PDU and EUT BMC type BMCs are all over the MNdh tree (*SI Appendix*, Fig. S2). This indicates that the function of MNdh is not tied to a specific BMC reaction pathway but more likely a very generic one. This is in stark contrast to a phylogenetic tree of the AldDh where a strong clustering of the sequences by BMC type is observed (1). Even the correlation with phylogenetic origin is not very strong, only a few phyla have their MNdh sequences clustered in one part of the tree, e.g., for Planctomycetes, Verrucomicrobia, and Elusimicrobia. This could indicate a frequent occurrence of horizontal gene transfer of the MNdh/BMC-TSE module and also supports our hypothesis of MNdh/BMC-T^{SE} having a function applicable to all AldDh containing BMC types. In some BMC types the MNdh/BMC-T^{SE} also occur more frequently in satellite loci (36) than main loci (PVM: 18 out of 20 occurrences are in satellite and 5 out of 7 for ACI), which suggests that they are a module that can be used under certain environmental conditions, such as anaerobic growth or specific redox conditions. In this way, MNdh/BMC-T^{SE} module contributes metabolic flexibility to a given BMC functional type.

Structural Modeling of MNdh and the MNdh-BMC-T^{SE} Complex. There are four distinct structural domains of MNdh: 1) the "Complex 1-51 kDa" pfam01512, 2) the soluble ligand binding β-grasp pfam10531, 3) the 4Fe-4S dicluster pfam13634, and 4) the RnfC sandwich hybrid domain pfam13375. As the name suggests, the pfam01512 domain is found in a protein of the respiratory complex 1 (e.g., NuoF in *Escherichia coli*); it covers the main part of the FMN/NAD binding domain. The four domains found in MNdh can be aligned with those in the RnfC subunit of the membrane-associated Rnf complexes [e.g. such as a Na+-translocating ferredoxin:NAD reductase (37)] as well as a subunit of the respiratory complex I [e.g., NuoF of *E. coli* (38)] (*SI Appendix*, Fig. S3). One notable difference is a circular permutation of the C-terminal pfam13375 domain that is instead found on the N terminus of both Rnf and respiratory I complex homologs.

We generated an AlphaFold2 model (39, 40) of MNdh based on the sequence of a *Clostridium botulinum* (*C. botulinum*) homolog (from a GRM1 type BMC; this protein was also used for experimental characterization, below) that shows a high level of confidence throughout (Fig. 2*A*). The *C. botulinum* MNdh is 40% identical (see *SI Appendix*, Fig. S3 for a sequence alignment) to the well-characterized PduS from *S. enterica*. We were able to place the 4Fe-4S clusters manually into the AlphaFold2 apo structure and the FMN and NAD+ using homologous structures (Fig. 2*B*). The AlphaFold2 model of MNdh closely resembles a recent Cryogenic electron microscopy (Cryo-EM) structure of RnfC, a Na+-translocating ferredoxin: NAD+ reductase (37) with no apparent effect of the circular permutation on overall structure (Fig. 2 *C* and *D*). Separating the RnfC into two parts and aligning each separately (to overcome the limitation of alignment tools to only consider contiguous alignment) gives rmsd values of 0.9 Å over 54 C-α atoms for the pfam13375 domain and 1.2 Å over 228 C-α atoms for the rest of the protein (*SI Appendix*, Fig. S4). The Fe-S clusters and the residues for the FMN/NADH binding site align very well (*SI Appendix*, Fig. S4, *Inset*). However, as expected, we see that a large number of differences between RnfC and MNdh are located at the interface region with their respective binding partners (Fig. 2 *C* and *D* and *SI Appendix*, Fig. S4, *Inset*).

We also generated an AlphaFold2 (41) prediction of a MNdh - BMC-T^{SE} complex (both from the *C. botulinum* sequences, Fig. 2*E*). The solutions obtained are largely identical to each other, indicating a good convergence; however from 25 solutions, half of them predict binding to the exterior of the shell via BMC-T^{SE}, the other half on the interior/lumenal surface as in Fig. 2*E* (Movie S1). The predicted binding to the concave, outside facing surface could be biased by a higher shape complementarity. Control docking simulations of MNdh to a BMC-H shell protein from the same operon show highly variable binding modes with a preference for the concave surface (Movie S2). Physiologically, the convex-surface binding (MNdh inside the BMC) is the most plausible, not only based on the function of internal NAD recycling but also because MNdh has been found in isolated intact BMCs (16, 42); noncovalent association of MNdh to the external surface of a BMC is unlikely to persist through purification. Further circumstantial evidence for an internal localization comes from much higher amino acid conservation observed for residues on the inside-facing convex surface, but only for the BMC-T^{SE} that co-occur with MNdh (*SI Appendix*, Fig. S5). In the BMC-T^{SE}-MNdh complex, the Fe-S cluster of BMC-T^{SE} is located along a straight line between the FMN/NADH binding site and the two Fe-S clusters of MNdh with only 7 to 9 Å between them (Fig. 2*E*), suggestive and of an electron transfer along this path analogous to the one seen in RnfC (37).

X-Ray Footprinting of the MNdh-BMC-T^{SE} Complex. To experimentally validate the AlphaFold2 model of the complex, we performed X-ray footprinting mass spectrometry (XFMS) on a purified *C. botulinum* MNdh-BMC-T^{SE} complex and BMC-T^{SE} alone, comparing the solvent-accessible residues between the complex and isolated BMC-T^{SE}. The samples were prepared anaerobically to preserve Fe-S cluster integrity, and the low oxygen conditions were maintained by rapidly loading them into an airtight sample environment for microsecond X-ray exposure. Hydroxyl radicals are generated by radiolysis isotropically wherever water is present; thus, when water is near side chain residues, they yield covalently modified hydroxylated or carbonylated product, which generally requires an oxygen environment but is also known to form under a low oxygen environment (43). We obtained near >95% sequence coverage for BMC-T^{SE}, and experiments in replicates exhibited consistent radiolytic labeling on identical residues. The hydroxyl radical reactivity rate constant was determined from the progressive extent of modification with an increase in the exposure time plots, which resembled the low oxygen environment for sample exposure (*SI Appendix*, Figs. S6 and S7 and Table S2). Those residues identified with changes in their modification rate in the complex MNdh-BMC-T^{SE}

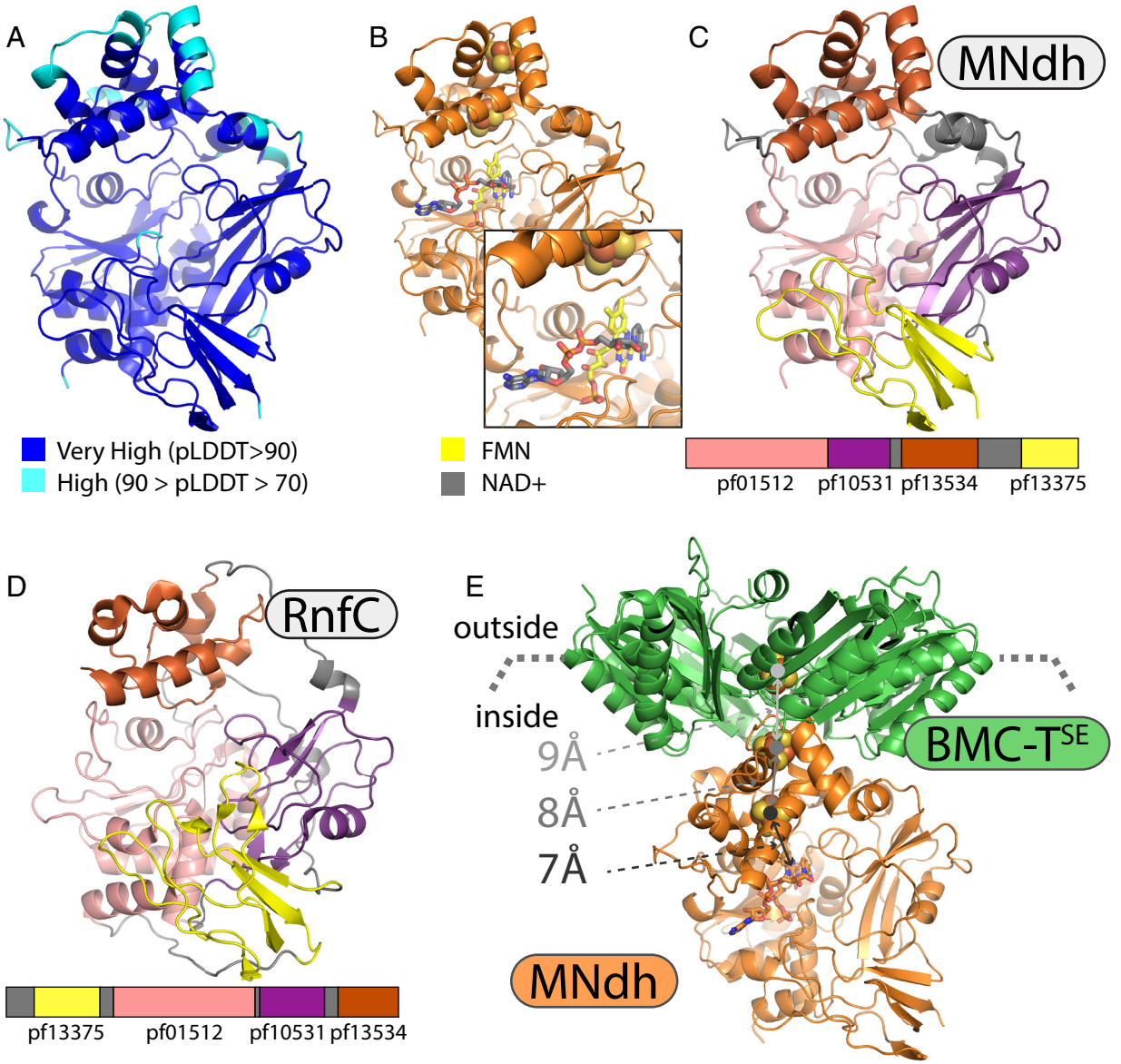

Fig. 2. Structural models of MNdh from *C. botulinum*. (*A*) AlphaFold2 confidence. (*B*) Cofactor and metal placement in the MNdh structure. (*C*) Domains of MNdh. (*D*) Domains of RnfC (*E*) Model of a MNdh-BMC-T^{SE} complex from *C. botulinum*.

vs. free BMC-T^{SE} are consequently likely to be involved in the conformational changes and interactions that mediate complex formation. The ratio of the site-specific rate constant of modification between isolated protein and complex provides the extent of solvent accessibility changes upon complex formation (Fig. 3). We divided the ratio of hydroxyl radical reactivities or changes in solvent accessibility into four categories. In the first category, Met23, Met100, and Met108, located in the hydrophobic core of individual subunits of BMC-T^{SE}, showed the highest decrease (more than 40-fold) in solvent accessibility. Buried Met residues have been reported to show some degree of hydroxyl radical reactivity due to the dynamic nature of the core, which can momentarily expose this highly reactive residue to the bulk water, giving rise to its hydroxyl radical modification product (44). However, here we observed almost complete protection of Met100 and Met108 upon formation of the complex. Since these residues project toward the same monomer core, between the beta-sheet and alpha helices of the BMC fold, these data indicate a nearly complete loss of dynamics upon MNdh binding, which could be due to a tightening of the interaction between subunits within the BMC-T^{SE} trimer upon binding MNdh. This is consistent with the disorder observed for the residues surrounding the pore in a crystal structure of the BMC-T^{SE} homolog PduT (45) where the absence of a binding partner might lead to an overall increased flexibility of the intramonomer and subunit interactions. Mutations of the pore cysteine residue have also been associated with increased permeability (46) which could be correlated higher flexibility of the residues surrounding the pore region.

The vast majority of changes in solvent accessibility were in the second category, and included residues at the intermonomer interface of the concave surface and intramonomer core: Met 7, Glu9, Pro123, Arg127, Leu132, Lys 135, Phe137, Ile151, Lys155, Leu164, Val169, Ile170, GLu179, Leu181, Leu 182. These residues showed a moderate decrease (~10 fold) in solvent accessibility, indicating an overall loss of water accessibility upon formation of the MNdh-BMC-T^{SE} complex. A similar loss of hydroxyl radical reactivity in the concave surface was observed previously in the formation of BMC heterohexamers (47). In the third category,

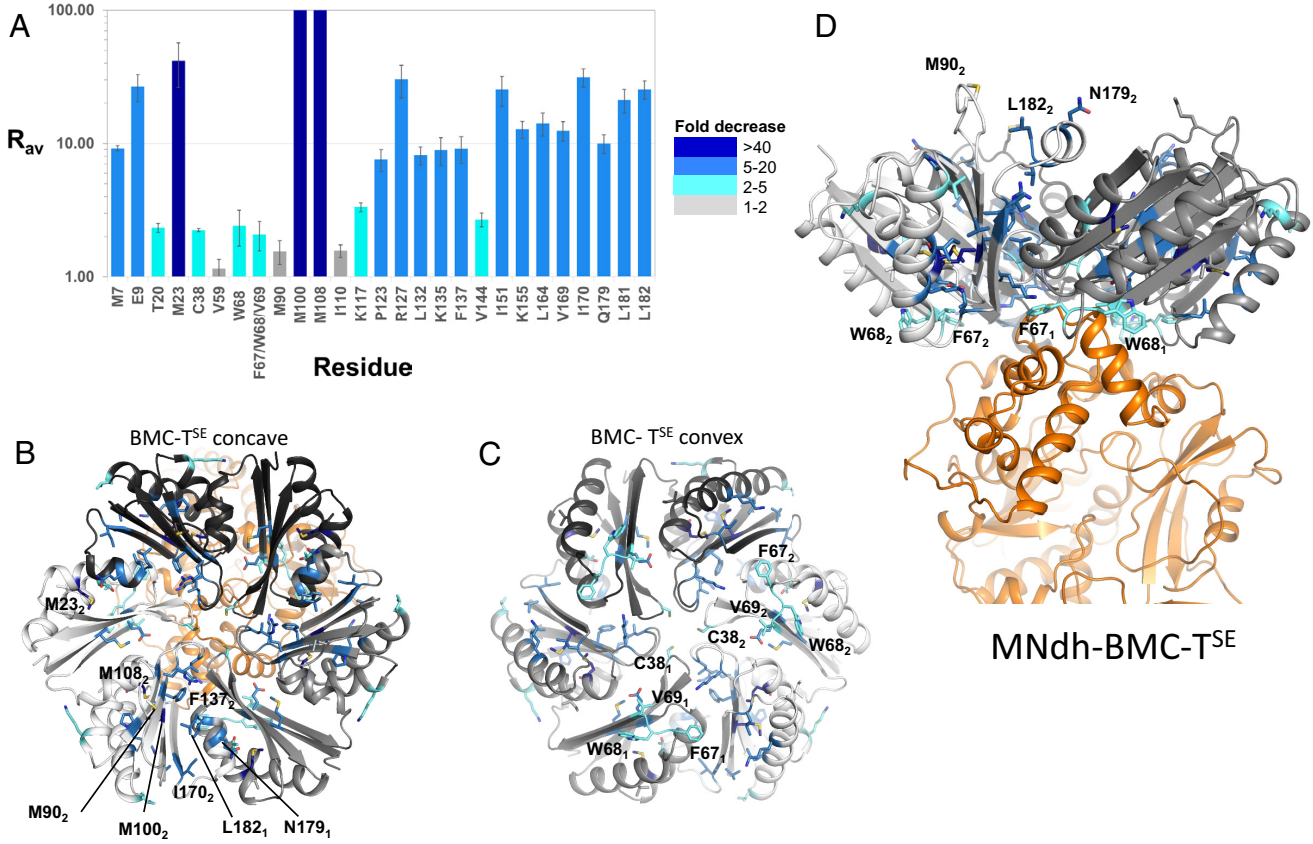

Fig. 3. Structural characterization of the MNdh-BMC-T^{SE} complex by X-ray footprinting. (*A*) Bar plot with color profile indicates fold change in the hydroxyl radical reactivity rate constant or solvent accessibility change between free BMC-T^{SE} and MNdh-BMC-T^{SE} complex. (*B–D*) Residues of the BMC-T^{SE} concave, convex, and side surface views are highlighted with the color profile in the bar plot and indicate fold change in solvent accessibility. Residue numbering follows the native protein sequence. Subscripts 1 and 2 highlight the asymmetric interaction of MNdh with BMC-T^{SE}; the solvent accessibility of residues involved in the interaction represent an average over all subunits.

residues Val59, Met90, and Ile110, which are not in direct contact with the subunit interface and MNdh, showed no change in solvent accessibility. In the fourth category, the residues Cys38, Phe67, Trp68, Val69, and three others (Thr20, Lys117, and Val144) showed only a ~threefold decrease in solvent accessibility (Fig. 3*B*). The AlphaFold2 model of the MNdh-BMC-T^{SE} complex indicates that only one out of three subunits of BMC-T^{SE} interact with MNdh near the Cys 38, Trp 68, Phe 67, and Val69 residues. XFMS reports on the protection pattern of the ensemble average under equilibrium conditions during the microsecond hydroxyl radical labeling reaction. Therefore, such nonspecific interactions will result in reduced sensitivity to differences in the reactivity rates and, thus, solvent accessibility changes. The approximate 1/3 solvent accessibility change at the hydrophobic cluster Phe 67-Trp 68-Val69 relative to the 10 fold change seen at the majority of residues supports the asymmetric interaction of MNdh with BMC-T^{SE} together with compaction of BMC-T^{SE} upon binding.

Characterization of a Purified MNdh-BMC-T^{SE} Complex. We coexpressed MNdh and BMC-T^{SE} from *C. botulinum* anaerobically with a histidine affinity tag on BMC-T^{SE}. A mutation of lysine 25 (numbering of untagged protein sequence) to glutamine for BMC-T^{SE} was engineered to prevent self-assembly that was observed for a native complex. Affinity purification followed by size exclusion chromatography under anaerobic conditions allowed us to isolate a stable complex containing both proteins (Fig. 4*A*) that contained FMN and Fe-S clusters (Fig. 4*B*).

The purified complex showed a rapid consumption of NADH, measured by absorption when we incubate the complex with the substrate aerobically. This reaction is dependent on an available electron acceptor which appears to be oxygen, as the reaction only proceeds in air and anaerobically sealed solutions do not show appreciable NADH conversion unless exposed to the aerobic environment (Fig. 4*D*). Using a series of substrate concentrations at low enzyme concentrations we were able to measure initial rates at determine a k_{cat} of 20 s^{-1} and a K_m of 0.98 mM for the reaction of NADH to NAD+ with oxygen as an electron acceptor (*SI Appendix*, Fig. S8*A*). This is in line with similar rates for RnfC (48); in this reaction, we do not know, however, if the transfer of the electrons to oxygen occurs at the FMN site or at any of the 4Fe-4S clusters (or a combination of them). The reaction as observed for complex I is likely occurring at the site of the FMN (49). For the oxygen to access the FMN it is likely necessary for the NAD(H) site to be empty; consistent with this hypothesis is the observed inhibition of the oxygen reaction by the presence of excess substrate or product (see 0.15 μM MNdh/O_2 trace in *SI Appendix*, Fig. S8*B* that plateaus after 120 s). From our model (Fig. 2*E*), either the BMC-T^{SE} Fe-S cluster or the FMN seem the most likely candidates as electron donors due to their solvent exposure. The NADH to NAD+ conversion reaction in absence of any other substrate however provides support for our hypothesis that MNdh is not directly involved in CoenzymeB_{12} regeneration.

In order to test our hypothesis of electron transfer, we analyzed samples of the MNdh/BMC-T^{SE} complex sing continuous wave (cw) X-band Electron Paramagnetic Resonance (EPR) spectroscopy;

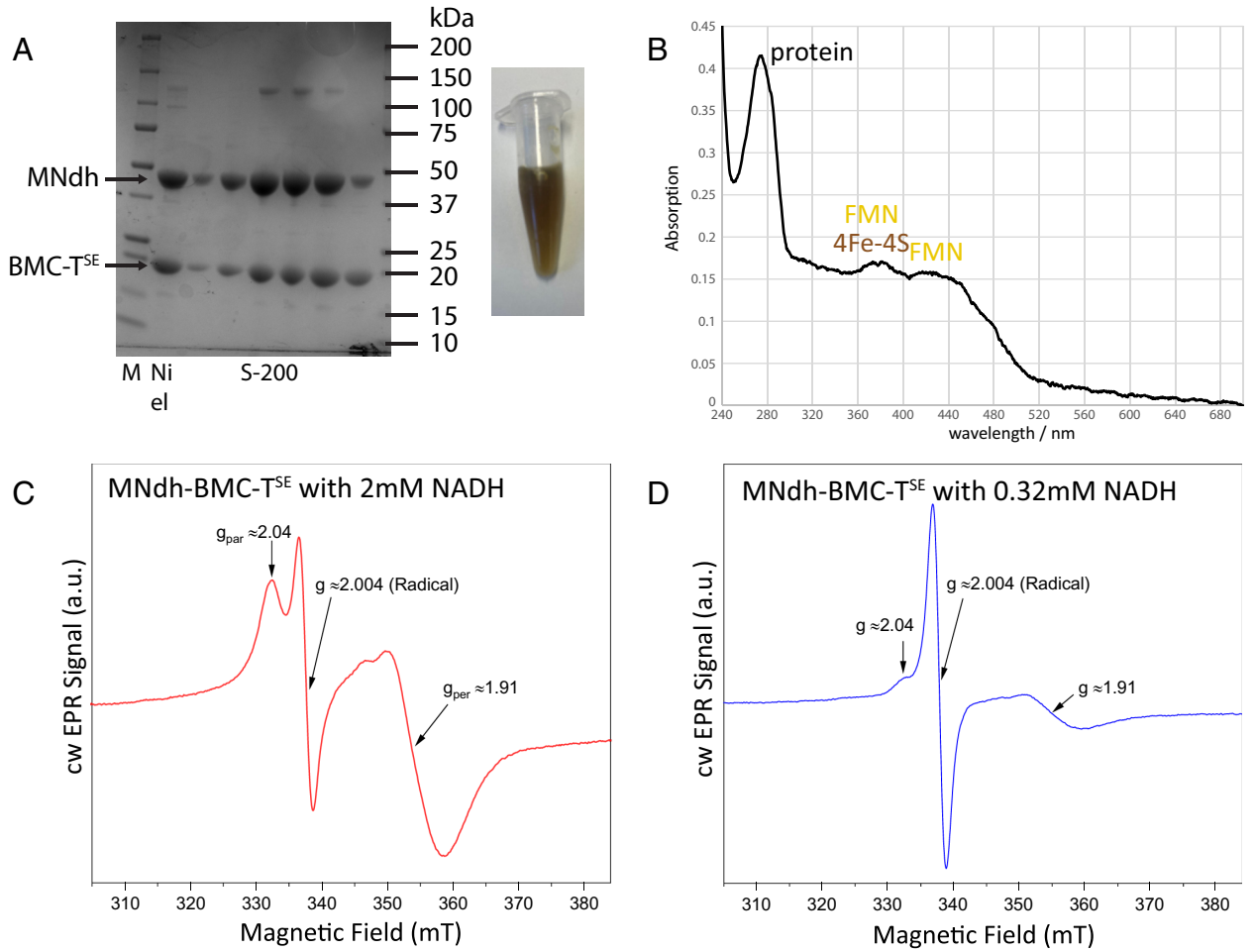

Fig. 4. Characterization of the MNdh-BMC-T^{SE} complex. (*A*, *Left*) Sodium dodecyl sulfate–polyacrylamide gel electrophoresis (SDS-PAGE) of complex as observed after Ni affinity purification followed by S-200 size exclusion chromatography. (*Right*) Color of purified complex indicates presence of Fe-S clusters and FMN cofactor. (*B*) Ultraviolet–visible (UV-vis) spectrum of the complex (5 μM), showing absorption peaks typical for 4Fe-4S clusters and oxidized FMN. (*C*) Continuous wave (cw) X-band EPR Spectra of 0.32 mM MNdh-BMC-T^{SE} complex reduced with 2 mM NADH (~7× molar excess), 3.2 mW microwave power, 1.2 mT modulation amplitude, 100 kHz modulation frequency, T = 10 K. (*D*) Same as *A* but MNdh-BMC-T^{SE} reduced with a stoichiometric amount of NADH (1:1). Note, that Fe-S Signal with g-factors $g_{par} \approx 2.04$ and $g_{per} \approx 1.91$, is not saturated at this microwave power, while organic radical signal with $g_r \approx 2.004$ is heavily saturated. Therefore, spin quantification for organic radical was done using EPR spectra recorded with significantly lower microwave power at higher temperature (*SI Appendix*, Fig. S9).

samples were prepared under anaerobic conditions. Addition of 2 mM (~7× stoichiometric excess) of the reductant NADH to the 0.32 mM protein solution leads to the appearance of a strong, broad, and fast relaxing signal characteristic for Fe-S clusters, with g-factors $g_{par} \approx 2.04$ and $g_{per} \approx 1.91$, and relatively small amount of organic radical with $g \approx 2.004$ as shown in Fig. 4*C*. The obtained g-values for the Fe-S cluster are in excellent agreement with previous EPR experiments (21) for BMC-T^{SE}. Importantly, these values are different from those reported for Fe-S clusters in PduS alone (32). Spin quantification of this Fe-S signal gave ≈ 0.17 mM, indicating that the reduction with NADH affected a substantial fraction of the protein. Concentration of the organic radical species was ≈0.007 mM which was determined by spin quantification of the spectra recorded at lower microwave power and higher temperature to avoid saturation behavior (*SI Appendix*, Fig. S9). This concentration is roughly 45× lower than the protein concentration, showing that the radical is also formed substoichiometrically. The linewidth (≈2 mT) and g-value (2.004) of this radical signal are in agreement with a reduced FMN radical (50).

Addition of a stoichiometric amount of NADH (0.32 mM) still leads to the appearance of Fe-S cluster signal with a concentration of ≈0.034 mM (Fig. 4*D*), which is ~five times less than in the 2 mM NADH sample. The g-values of the Fe-S cluster signals in the two samples are similar, indicating that the same Fe-S cluster, i.e., the BMC-T^{SE} one, was reduced (Fig. 4*D*). A much stronger organic radical signal was observed in this sample and spin quantification gave 0.034 mM vs. 0.007 mM spins (~five times stronger than the former sample). This implies that radical and Fe-S signals are formed in equal amount in about 1/10th of the proteins. The 1:1 ratio of radical to Fe-S signals in the sample reduced stoichiometrically with NADH can be explained by double reduction of FMN by NADH. Doubly reduced FMN (including its double protonated form $FMNH_2$) is in a singlet spin state and thus cannot be observed by EPR. Further electron transfer to the Fe-S clusters of MNdh leads to the appearance of two EPR signals: one from singly reduced FMN radical and another one from singly reduced Fe-S cluster with stoichiometric ratio of 1:1.

To measure electrochemical properties of both FMN and the Fe-S clusters, we analyzed samples of the MNdh-BMC-T^{SE} complex using protein film square-wave voltammetry (SWV). Background-corrected SWVs of MNdh-BMC-T^{SE} reveal several overlapping redox peaks whose relative peak heights increase unevenly with increasing pulse frequency (Fig. 5*A*), thereby enabling deconvolution and identification of five distinct redox waves. This is consistent with three one-electron reductions associated with each Fe-S cluster, and two sequential one-electron reductions associated with FMN. Because FMN undergoes two

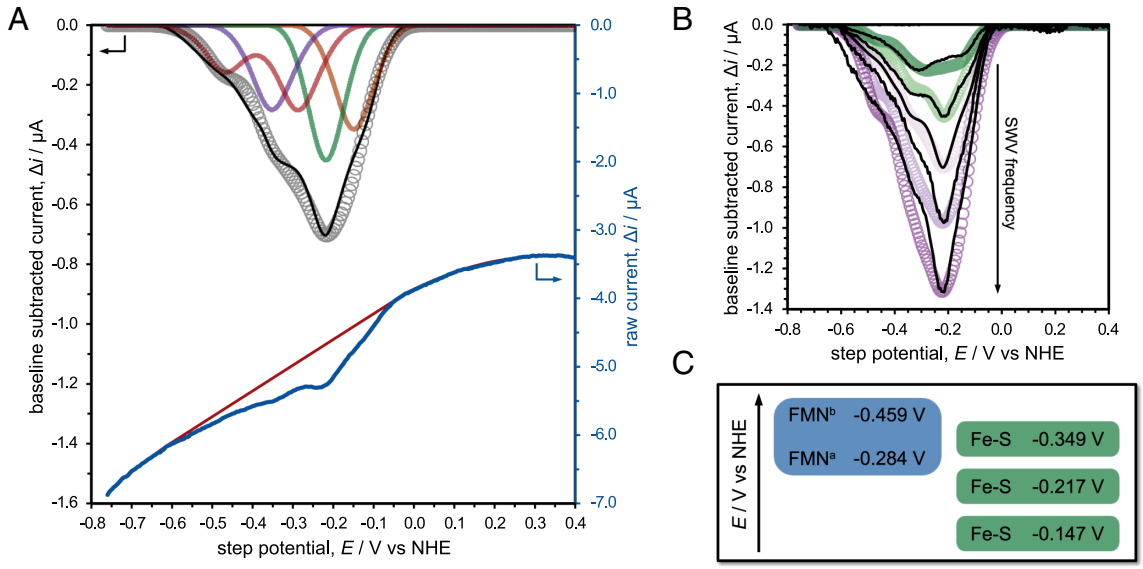

Fig. 5. (*A*) Representative protein film SWV of MNdh-BMC-T^{SE} complex (solid blue = raw current, solid red = background current, solid black = background-corrected current) and a SWV simulated using DigiElch (open gray circles) with its composite peaks (red, purple, green, and orange solid curves). Simulated SWVs are composed of four surface-confined species and five total redox waves: 3× reversible one-electron waves (orange, green, and purple curves) corresponding to Fe-S clusters and 2× coupled one-electron EE waves (red curve) corresponding to the flavin. (*B*) Experimental (solid black curves) and simulated (open circles) protein film SWVs of MNdh-BMC-T^{SE} complex at potential pulse frequencies of 5 Hz, 10 Hz, 20 Hz, 30 Hz, and 40 Hz. (*C*) Scheme illustrating the assigned redox potential for the Fe-S clusters and the first (FMN^a = quinone/semiquinone) and second (FMN^b = semiquinone/hydroquinone) redox potentials of the FMN cofactor. Electrochemical experiments were performed with a pulse height of 20 mV, step height of 5 mV, and frequency of 20 Hz (for *A*) using a 4-(2-hydroxyethyl)-1-piperazineethanesulfonic acid (HEPES)-buffered saline solution under N_2 at pH 7 and 25 °C.

sequential proton-coupled electron transfer steps, it can be modeled as a single adsorbed redox species and distinguished from the Fe-S clusters. Experimental protein film SWVs were fit to SWVs simulated using DigiElch and are in good agreement with a surface-confined model consisting of three one-electron reductions—standard reduction potentials of −0.147 V, −0.217 V, and −0.349 V (assigned here as the Fe-S clusters)—and two coupled one-electron reductions—standard reduction potentials of −0.284 V and −0.459 V (assigned here as the quinone/semiquinone and semiquinone/hydroquinone forms of FMN). Furthermore, simulated SWV curves were fit with experiments across multiple frequencies using constant simulation parameters and were found to be in good agreement ($R^2 > 0.98$ for all frequencies studied, Fig. 5*B*).

Control SWV experiments performed using thermally denatured MNdh-BMC-T^{SE} reveal a single redox peak at −0.205 V consistent with free FMN (51, 52), suggesting that SWV peaks observed with intact MNdh-BMC-T^{SE} are not the result of fully denatured protein. Additionally, SWVs of partially denatured MNdh-BMC-T^{SE} (brief exposure to aerobic conditions to react the Fe-S clusters) reveal the loss of peaks at −0.147, −0.217, and −0.349 V while the peaks assigned to FMN (−0.284 V and −0.459 V) were unchanged (*SI Appendix*, Fig. S10). Taken together, these data are consistent with the proposed assignment of redox peaks. Based on the assigned redox potentials, the first electron transfer from doubly reduced FMN to Fe-S is significantly more favorable than the second electron transfer from the semiquinone form. This relatively stable semiquinone may further explain the comparatively high concentration of organic radical observed by EPR after reaction with stoichiometric NADH. While formation of the stable semiquinone may not be relevant to the physiological function, shifts in the redox potentials when the complex is assembled into a shell and/or upon substrate binding could eliminate significant formation of the radical species.

Discussion

The initial characterization of PduS, a MNdh homolog in PDU BMCs proposed a function as a regenerating enzyme for adenosylcobalamin/Coenzyme B_{12} (32); however, this cofactor is only required in the signature enzymes of the EUT and PDU BMCs. However, MNdh is widespread among BMCs and Coenzyme B_{12} does not seem to be a cofactor in any other characterized BMC types, nor is there evidence of B_{12} binding motifs in protein sequences associated with uncharacterized BMC types. The widespread occurrence of MNdh/BMC-T^{SE} across BMC types as well as across phyla (*SI Appendix*, Fig. S1) strongly implies an alternative, more universal function. This would be consistent with a recent observation by Burrichter et al. (16) that found a homolog of MNdh in a purified taurine-degrading BMC and speculated that it could be involved in electron transfer via a BMC-T^{SE} protein. An involvement of MNdh in B_{12} regeneration is not necessarily mutually exclusive with NAD+ regeneration but the B_{12}-associated function might be an indirect one as proposed at the time of initial PduS characterizations (53).

There are five substantial pieces of evidence to support the function of MNdh as a housekeeping NAD+ regenerating BMC enzyme. I) It is present in many types of BMCs that catabolize different substrates; these all contain AldDh; and many observations (361) in which the next step in the metabolosome paradigm catalyzed by alcohol dehydrogenase, with its required function of NAD recycling, is missing. II) Homology to the function of structurally related enzymes RnfC and NuoF and high structural alignment over the whole sequence between RnfC and MNdh with little room for binding alternate cofactors such as cobalamin. III) Distribution of MNdh and BMC-T^{SE} sequences on a phylogenetic tree is not correlated with BMC type, indicating a more general function unrelated to a specific substrate (*SI Appendix*, Fig. S2). IV) Strict co-occurrence of MNdh with BMC-T^{SE} (but not vice versa), highlighting the need for electrons to be passed to the outside if MNdh is present in the BMC. V) Functional assays

support the function of NAD+ regeneration in vitro without the need for additional substrates like Coenzyme B_{12}.

There are likely a multitude of ways for cofactor regeneration in BMCs; at low throughput and with a high-enough concentration gradient, BMCs might even work with cofactor exchange across the shell through some of the larger pores in BMC-T^S shell proteins. Many of the BMC loci that contain MNdh also contain an alcohol dehydrogenase (Fig. 1*C* and *SI Appendix*, Table S1). Their functions are seemingly redundant, but complementary if dependent on redox condition. The MNdh reaction is likely faster since it only needs NADH to bind and not an additional substrate. Both the alcohol dehydrogenase as well as MNdh (PduS in PDU BMCs) have been analyzed in the *Salmonella* PDU system with genetic knockouts (7, 34). Despite the apparent necessity of an alcohol dehydrogenase for cofactor recycling inside the BMC, a PduQ (alcohol dehydrogenase) knockout was found to still grow on the PDU substrate 1,2-propanediol at 79% of the wildtype rate (7). Our proposed function for MNdh elegantly accounts for this activity that otherwise could only be explained with substantial amounts of NAD+/NADH transfer across the shell membrane. Likewise, the PduS knockout was found to also affect the growth rate (34) but does not abolish growth. Similarly, a PduT knockout only slightly affected the growth rate (54). This indicates that for *Salmonella* PDU BMCs under commonly used growth conditions, it is likely that both NAD+ regeneration systems are utilized. The redundancy attests to the importance of cofactor recycling for function of the BMC.

The observation of oxygen as a potential electron acceptor could provide a means to remove oxygen inside the BMC. Both MNdh and the alcohol dehydrogenase are sensitive to oxygen (7, 32). However, using oxygen as an electron acceptor results in reactive oxygen species but those might react nonspecifically with proteins rather than with the sensitive Fe-S clusters. The strict co-occurrence of MNdh with BMC-T^{SE} (*SI Appendix*, Table S1) suggests that they are both needed to fulfill the function of MNdh. This is consistent with our model of a linear electron transfer of two electrons from NADH to the FMN cofactor of MNdh and then through the two Fe-S clusters to the Fe-S cluster of BMC-T^{SE}. We support this path and directionality with EPR measurements (Fig. 4 *C* and *D*) and protein voltammetry (Fig. 5 *A* and *B*). The distances between the Flavin and iron-sulfur clusters are short enough to allow this (Fig. 2*E*). Experimentally in vitro, we have established oxygen as an electron acceptor (*SI Appendix*, Fig. S8 *C* and *D*), however in vivo it is likely that a small redox protein, such as a ferredoxin or flavodoxin which could access the Fe-S cluster in the center of the concave BMC-T^{SE} pore are the final acceptors. There are a number of pfam02441 Flavoprotein type proteins in MNdh-encoding BMC operons and it is possible that some of those could act as electron acceptors. However, those are also found in loci that do not contain MNdh, such as for the characterized flavodoxin from a PDU1C BMC locus (55). The lack of a specific protein that co-occurs with MNdh/BMC-T^{SE} indicates that the interaction of BMC-T^{SE} with the acceptor is likely not very specific and different molecules are able to receive the electrons across the variety of species that MNdh/BMC-T^{SE} occur in. The lack of specificity is in line with what has been observed for soluble electron carriers in general (56). It is however possible that oxygen can fill the role of electron acceptor in vivo as well. If this reaction occurs in proximity to the BMC that might be beneficial to protect other enzymes that are highly sensitive to oxygen such as the glycyl radical enzymes that undergo proteolytic cleavage when reacting with oxygen (57). Oxygen as an electron acceptor has been observed for respiratory complex I in mitochondria and has major health implications due to the generation of superoxide, leading to cellular oxidative stress (58).

There are a number of metabolosome BMC loci that contain neither of the regeneration systems, such as in the ARO, EUT3, MIC2/3, PVMlike, RMM/AAUM, and SPU6 BMC types (36); how NAD+ regeneration is achieved for those cases has yet to be determined. Additional potentially redundant mechanisms for cofactor recycling underscores the importance of its maintenance for the function of these megadalton metabolic machines. There are also BMC types that do not have an AldDh such as the proposed Xanthine degrading BMC (59) where MNdh/BMC-T^{SE} are not found and there is no evidence of involvement of NADH for the reaction mechanism. Future work on specific BMC types should consider the mechanism for cofactor regeneration, which is just as important as reaction pathways to explain the biochemistry occurring inside the BMC. The MNdh as a NAD+ regenerating enzyme improves the efficiency of the reactions by removing the need for an alcohol dehydrogenase which generates an alcohol side product for each turnover of the main substrate. The possibility of alternate electron acceptors, used under different physiological conditions, for this shell-associated module suggests that it confers metabolic flexibility, which at the next step in the scale of organization is the hallmark metabolosome function. The new function of this enzyme in BMCs also established the BMC shell as a separating membrane for cofactor pools and a conduit for electrons. This extends previous work on engineering metal centers into the pores of BMC shell proteins (35, 60) and sets the stage for connecting redox functions between the inside and outside of BMC shells.

Materials and Methods

Cloning, Protein Expression, Purification, and Activity Assays. We have designed an *E. coli* codon optimized gene for MNdh and BMC-T^{SE} from the GRM1 operon of *C. botulinum* E3 strain Alaska E43; see sequences in *SI Appendix*, Table S3. The BMC-T^{SE} sequence contains an N-terminal his-tag and a mutation of the "antiparallel" lysine 25 (numbering of untagged protein sequence) to glutamine to prevent self-assembly. The open reading frames were cloned into a pACYCDuet vector using Gibson cloning.

The plasmid was transformed into a ΔiscR *E. coli* BL21(DE3) strain [that lacks *iscR*, the negative repressor of the isc operon that is involved in the biogenesis of cellular iron-sulfur proteins, in order to improve Fe-S cluster formation (61)] for expression. 1.5 L LB broth medium with 0.5% glucose and buffered with 100 mM MOPS/NaOH pH 7.4 was inoculated with 20 mL of an overnight preculture and grown in a 2 L bottle in a shaking incubator at 120 rpm and 37 °C. At OD_{600} of 0.6 to 0.8 the culture was sparged with nitrogen and the medium was supplemented with L-cysteine at 2 mM, sodium fumarate at 25 mM, ferric ammonium citrate at 2 mM and Isopropyl β-d-1-thiogalactopyranoside (IPTG) at 0.25 mM final concentration. The flask was then sealed and grown overnight at 30 °C. Cells were harvested by centrifugation at 7,000 × *g* for 7 min and either processed immediately or frozen at −20 °C until purification. For purification, the cell pellet from a 1.5 L culture was resuspended in 20 mL buffer A (20 mM phosphate pH 7.0, 50 mM NaCl, 20 mM imidazole). 200 µL 2 mg/mL DNase I was added as well as ½ tablet of Ethylenediaminetetraacetic acid (EDTA)-free protease inhibitor (Roche). The cell suspension was lysed by two passages of a French Press at 25,000 psi, and the lysate was then cleared with a 20,000 × *g* spin for 30 min. The soluble lysate was then transferred into a Coy anaerobic glove box under 2.5% hydrogen/nitrogen atmosphere and applied onto a 5 mL HiTrap HP Ni-NTA resin, washed with 40 mL buffer A and eluted with buffer B (20 mM phosphate pH 7.0, 50 mM NaCl, 300 mM imidazole). The elution fraction was then concentrated to 500 µL using an Amicon concentrator with a 30 kDa molecular weight cutoff (MWCO) and manually injected on a Superdex S-200 10/300 column equilibrated in 10 mM PBS pH 7.0 and 50 mM NaCl, and elution fractions were collected manually. Purification of BMC-T^{SE} alone was performed with the same protocol. Fractions were analyzed on SDS-PAGE and if necessary concentrated using and Amicon 30 kDa MWCO concentrator. For enzymatic parameter determination assays, the protein was used at 4 nM with NADH concentrations between 50 µM to 750 µM in a 96-well plate with 100 µL volume per well and three replicates. The reaction

was started by mixing protein and NADH with a large excess of aerobic buffer. Absorption at 340 nm was tracked using a Tecan Spark. The UV–Vis spectrum is an average of three traces of at 5 μM complex sample. Protein concentrations were determined using a Bicinchoninic acid assay (BCA) assay with a bovine serum albumin (BSA) standard curve.

Bioinformatic Analysis. The locus and protein sequence database from Sutter et al. (1), available also as a web interface (36), was used for all analysis. Protein sequences were of MNdh were aligned with ClustalW (62) trimming with trimAl 1.2rev59 (63) with parameters -gt 0.6 -cons 30 -w 3. The sequence alignment was then used to construct a maximum likelihood tree using RAxML-NG (v0.6.0) (64). Trees were examined and visualized using Archaeopteryx (www.phylosoft.org/archaeopteryx). Co-occurrence data were extracted from the locus data (from ref. 1 and also included as Dataset S1) using a simple python script that determines whether the two determining HMMs for MNdh are present and adjacent (HMMS are identified uniquely by a "HMMPduS" string or a position sensitive "Ts_" query). 97% (2,105 loci) of the MNdh occur right next to a BMC-T^{SE} on the genome, 1.8% (39 loci) one gene in between, 0.1% (three loci) more than two genes away, 1.2% (25 loci) no BMC-T^{SE} in locus. Pore cysteine motifs were found on all the BMC-T^{SE} pairing with MNdh (MNdh and BMC-T^{SE} sequences can also be found in Dataset S1).

Structural Modeling. The structure for the *C. botulinum* MNdh-BMC-T^{SE} complex was predicted using AlphaFold multimer (40, 65), as distributed in version 2.3.1 of AlphaFold. The prediction used the defaults with the full AlphaFold database and a template date of January 1st 2022. AlphaFold predicted the BMC-T^{SE} trimer based on strong homology to existing solved structures for trimeric shell proteins. MNdh had fewer clear homologs in the PDB, but AlphaFold yields pLDDT scores above 70, and typically 90 or better (Fig. 2*A*). AlphaFold predicts that the MNdh monomer can be placed on either side of the trimer (Movie S1). Based on the anticipated localization for catalysis within the shell, only the model where the MNdh was inside in the context of a BMC shell was considered realistic. A control docking of MNdh with a hexamer from the same *C. botulinum* operon (sequence listed in *SI Appendix*, Table S3) did not show discrete orientations (Movie S2). Fe-S- clusters could be inserted manually in the AlphaFold apo structure with reasonable Cys-Fe distances. FMN and NAD+ were placed based on a structural alignment with the crystal structure of NuoF (pdb ID 6HL3), which contains both molecules. Protein structures were visualized with PyMOL (The PyMOL Molecular Graphics System, version 2.5.4 Schrödinger, LLC).

X-Ray Radiolysis and Mass Spectrometry. Radiolysis of 8 μM BMC-T^{SE} and MNdh- BMC-T^{SE} samples were performed at the Advanced Light Source (ALS) beamline 3.3.1, which delivers a 3 to 12 keV broadband X-ray beam from a bending magnet source with a high flux density focused beam. We used an X-ray slit to produce a beam size at full-width-half-max of 640 μm (vertical) × 200 μm (horizontal) for sample exposure using a 200 μm ID capillary. Samples were loaded into a gas-tight lure lock Hamilton glass syringe and ejected through a 640 μm X-ray path using a 200 μm ID capillary at various speeds to achieve an exposure range of 400 to 1,600 μs. Exposed sample was collected in tubes containing 60 mM methionine amide to immediately scavenge any secondary radical reaction products. The protein samples were cysteine alkylated and digested in trypsin and Glu-C using standard procedures (66). LCMS was conducted on a Thermo Scientific Q Exactive Orbitrap Mass Spectrometer coupled to a Thermo Scientific UltiMate 3000 RSLCnano system. Digested samples were separated on a C18 column with a 15 min acetonitrile/0.1% formic acid gradient as follows: ~1 to 10% over 2.5 min, ~10 to 40% over 12.5 min, and ~40 to 90% over 1 min. Peptides were analyzed in positive mode with data-dependent MS/MS using HCD fragmentation. Instrument control was via Xcalibur 4.1. XFMS peptide identification and analysis has been automated and enhanced by adopting the Byos® (Protein Metrics Inc.) integrated software platform as previously described (67). Biologic automatically extracts ion chromatograms and reports the quantification of modifications relative to the unmodified peptide based on the extracted ion chromatograms. A typical workflow starts with processing a high-exposure tandem MS (MS/MS) file in Byos for an MS/MS search against FASTA sequences and the localization of modification sites. The peptide level analysis and validation of assignments are carried out in Byologic and lead to the creation of in silico peptides in the form of a CSV file using the MS/MS data. The in silico peptides CSV is subsequently applied to full scan (MS1) data covering a series of exposure times, and the resulting quantified peptide modifications provide the basis for the residue-specific and peptide-level dose–response. The abundance (peak area) of the identified unmodified and modified peptides at each irradiation time point area were measured from their respective extracted ion chromatogram of the mass spectrometry data collected in the precursor ion mode. The fraction unmodified for each peptide was calculated as the ratio of the integrated peak area of the unmodified peptide to the sum of integrated peak areas from the modified and unmodified peptides. The dose–response curves (fraction unmodified vs. X-ray exposure) were fitted to single exponential functions in Origin® Version 9.0 (OriginLabs). The rate constant, k (s^{-1}), was used to measure the reactivity and solvent accessibility of sidechains toward hydroxyl radical-induced modification (*SI Appendix*, Figs. S6 and S7). The ratio of rate constants provided the relative change in the solvent accessibility between the free protein and the complex.

EPR Spectroscopy. Samples for EPR spectroscopy were prepared as above; the size exclusion peak fractions were concentrated to 0.2 to 0.3 mM (protein concentrations determined by BCA assay) using an Amicon spin concentrator and shipped/stored on ice until use. The EPR sample manipulation was done in a N_2 glovebox to minimize damage due to oxygen exposure. The samples were filled into 4 mm o.d. thick-walled Suprasil X-band EPR tubes. Continuous wave (cw) X-band (9.5 GHz) EPR experiments were performed on a Bruker ELEXSYS II E500 EPR spectrometer (Bruker BioSpin, Ettlingen, Germany), equipped with a TE_{102} rectangular EPR resonator (Bruker ER 4102ST). The phase-sensitive detection with field modulation leads to first derivative type spectra, not the absorptive type spectra typically observed in other spectroscopic methods. All measurements were performed at cryogenic temperatures (10 to 30 K). A helium gas-flow cryostat (ICE Oxford, UK) and an ITC503 (Oxford Instruments, UK) were used for measurements at cryogenic temperatures. Data processing was performed using Xepr (Bruker BioSpin, Ettlingen) and Matlab (The MathWorks, Inc., Natick, Massachusetts, USA) software. Determination of the spin concentrations were done using the SpinCount application implemented in the Xepr software. Note that Fe-S signal at 10 K was not saturated at the microwave powers used in this study. The organic radical signal was strongly saturated at 10 K. For this reason the spin quantification of the organic radical was performed at T = 20 K, low microwave power, 6 μW, and small modulation amplitude, 0.4 mT (*SI Appendix*, Fig. S9).

Protein Film Square Wave Voltammetry. Electrochemical experiments were performed using a BioLogic VMP potentiostat with a 3 mm glassy carbon working electrode, a Pt wire counterelectrode, and Ag/AgCl reference electrode. Reference potentials were adjusted to the normal hydrogen electrode by adding 0.205 V. Working electrodes were cleaned and prepared following a protocol adapted from Plegaria et al. (60). Electrodes were washed by sonication and subsequent rinsing with Milli-Q water. Protein film electrodes were prepared by drop casting 10 μL of 10 mg/mL protein onto the electrode surface under a N_2 environment and allowing them to dry over 15 to 30 min. Square wave voltammetry experiments were performed using 75 mM HEPES buffer with 150 mM NaCl at 25 °C under N_2 atmosphere unless otherwise specified. Square wave voltammograms were performed from 0.2 V to −1.0 V vs Ag/AgCl with a step height of 5 mV, a pulse height of 20 mV, and pulse widths of 200, 100, 50, 33, and 25 ms (corresponding to 5, 10, 20, 30, and 40 Hz). For thermally denatured samples, protein was denatured at 95 °C for 15 min before being drop cast and measured as above. Electrochemical data were processed (background subtraction and curve smoothing) using QSoas 3.2 (68).

Electrochemical simulations were performed using DigiElch 7.0 software. Protein films were modeled as surface-confined redox processes in a manner described by Mayall et al. (69). Assuming that all species have the same surface concentration (i.e., cofactor stoichiometry is conserved on the electrode surface), the observed changes in relative peak heights with changes in pulse frequency can be attributed to differences in electron transfer rate constants between each cofactor and the electrode. A constant surface coverage was used for all simulations of $\Gamma = 1.87 \times 10^{-11}$ mol cm^{-2}, while heterogeneous rate constants and redox potentials for each species were fit to the experimental SWV data.

Data, Materials, and Software Availability. All study data are included in the article and/or supporting information.

ACKNOWLEDGMENTS. We thank Jasleen K. Bindra for help with the EPR measurements and Kalpana Singh for help with activity assays. This work was

supported as part of the Center for Catalysis in Biomimetic Confinement, an Energy Frontier Research Center funded by the U.S. Department of Energy (DOE), Office of Science, Basic Energy Sciences under Award Number DE-SC0023395 after preliminary support from the U.S. DOE, Office of Science, Basic Energy Sciences under Award Number DE-FG02-91ER20021. The ALS at Lawrence Berkeley National Laboratory is supported by the Director, Office of Science, Office of Basic Energy Sciences, U.S. DOE under Contract DE-AC02-05CH11231. The EPR work is supported by the U.S. DOE, Office of Science, Office of Basic Energy Sciences, Division of Chemical Sciences, Geosciences, and Biosciences, through Argonne National Laboratory under Contract No. DE-AC02-06CH11357. The ALS and the Molecular Foundry are supported by the Office of Science of the U.S. DOE under contract DE-AC02-05CH11231. XFMS work was supported by NIH R01 GM126218 and NIH P30 GM124169.

Author affiliations: [a]MSU-DOE Plant Research Laboratory, Michigan State University, East Lansing, MI 48824; [b]Environmental Genomics and Systems Biology Division, Lawrence Berkeley National Laboratory, Berkeley, CA 94720; [c]Molecular Biophysics and Integrated Bioimaging Division, Lawrence Berkeley National Laboratory, Berkeley, CA 94720; [d]Chemical Sciences and Engineering Division, Argonne National Laboratory, Lemont, IL 60439; [e]Molecular Foundry Division, Lawrence Berkeley National Laboratory, Berkeley, CA 94720; [f]Biophysics Graduate Program, University of California, Berkeley, CA 94720; [g]Department of Biochemistry and Molecular Biology, Michigan State University, East Lansing, MI 48824; and [h]Department of Chemical Engineering and Materials Science, Michigan State University, East Lansing, MI 48824

1. M. Sutter *et al.*, A catalog of the diversity and ubiquity of bacterial microcompartments. *Nat. Commun.* **12**, 3809 (2021).
2. C. A. Kerfeld, C. Aussignargues, J. Zarzycki, F. Cai, M. Sutter, Bacterial microcompartments. *Nat. Rev. Microbiol.* **16**, 277–290 (2018).
3. A. Turmo, C. R. Gonzalez-Esquer, C. A. Kerfeld, Carboxysomes: Metabolic modules for CO_2 fixation. *FEMS Microbiol. Lett.* **364**, fxn176 (2017).
4. S. D. Axen, O. Erbilgin, C. A. Kerfeld, A taxonomy of bacterial microcompartment loci constructed by a novel scoring method. *PLoS Comput. Biol.* **10**, e1003898 (2014).
5. K. L. Stewart, A. M. Stewart, T. A. Bobik, Prokaryotic organelles: Bacterial microcompartments in E. coli and Salmonella. *EcoSal Plus* **9** (2020), 10.1128/ecosalplus.ESP-0025-2019.
6. C. A. Kerfeld, O. Erbilgin, Bacterial microcompartments and the modular construction of microbial metabolism. *Trends Microbiol.* **23**, 22–34 (2015).
7. S. Cheng, C. Fan, S. Sinha, T. A. Bobik, The PduQ enzyme is an alcohol dehydrogenase used to recycle NAD+ internally within the Pdu microcompartment of Salmonella enterica. *PLoS One* **7**, e47144 (2012).
8. E. Kofoid, C. Rappleye, I. Stojiljkovic, J. Roth, The 17-gene ethanolamine (eut) operon of Salmonella typhimurium encodes five homologues of carboxysome shell proteins. *J. Bacteriol.* **181**, 5317–5329 (1999).
9. T. A. Bobik, G. D. Havemann, R. J. Busch, D. S. Williams, H. C. Aldrich, The propanediol utilization (pdu) operon of Salmonella enterica serovar Typhimurium LT2 includes genes necessary for formation of polyhedral organelles involved in coenzyme B12-dependent 1,2-propanediol degradation. *J. Bacteriol.* **181**, 5967–5975 (1999).
10. O. Erbilgin, K. L. McDonald, C. A. Kerfeld, Characterization of a planctomycetal organelle: A novel bacterial microcompartment for the aerobic degradation of plant saccharides. *Appl. Environ. Microbiol.* **80**, 2193–2205 (2014).
11. J. Zarzycki, O. Erbilgin, C. A. Kerfeld, Bioinformatic characterization of glycyl radical enzyme-associated bacterial microcompartments. *Appl. Environ. Microbiol.* **81**, 8315–8329 (2015).
12. J. Zarzycki, M. Sutter, N. S. Cortina, T. J. Erb, C. A. Kerfeld, In vitro characterization and concerted function of three core enzymes of a glycyl radical enzyme–Associated bacterial microcompartment. *Sci. Rep.* **7**, 42757 (2017).
13. H. S. Schindel, J. A. Karty, J. B. McKinlay, C. E. Bauer, Characterization of a glycyl radical enzyme bacterial microcompartment pathway in. *J. Bacteriol.* **201**, e00343-18 (2019).
14. A. P. Lundin *et al.*, Genetic characterization of a glycyl radical microcompartment used for 1,2-propanediol fermentation by uropathogenic Escherichia coli CFT073. *J. Bacteriol.* **202**, e00017-20 (2020).
15. E. Mallette, M. S. Kimber, Structural and kinetic characterization of (S)-1-amino-2-propanol kinase from the aminoacetone utilization microcompartment of Mycobacterium smegmatis. *J. Biol. Chem.* **293**, 19909–19918 (2018).
16. A. G. Burrichter *et al.*, Bacterial microcompartments for isethionate desulfonation in the taurine-degrading human-gut bacterium Bilophila wadsworthia. *BMC Microbiol.* **21**, 340 (2021).
17. M. N. Xing *et al.*, Radical-mediated C-S bond cleavage in C2 sulfonate degradation by anaerobic bacteria. *Nat. Commun.* **10**, 1609 (2019).
18. L. Doron, M. Sutter, C. A. Kerfeld, Characterization of a novel aromatic substrate-processing microcompartment in Actinobacteria. *mBio* **14**, e0121623 (2023).
19. M. F. Slininger Lee, C. M. Jakobson, D. Tullman-Ercek, Evidence for improved encapsulated pathway behavior in a bacterial microcompartment through shell protein engineering. *ACS Synth. Biol.* **6**, 1880–1891 (2017).
20. C. Chowdhury *et al.*, Selective molecular transport through the protein shell of a bacterial microcompartment organelle. *Proc. Natl. Acad. Sci. U.S.A.* **112**, 2990–2995 (2015).
21. J. B. Parsons *et al.*, Biochemical and structural insights into bacterial organelle form and biogenesis. *J. Biol. Chem.* **283**, 14366–14375 (2008).
22. C. E. Mills *et al.*, Vertex protein PduN tunes encapsulated pathway performance by dictating bacterial metabolosome morphology. *Nat. Commun.* **13**, 3746 (2022).
23. M. Sutter, B. Greber, C. Aussignargues, C. A. Kerfeld, Assembly principles and structure of a 6.5-MDa bacterial microcompartment shell. *Science* **356**, 1293–1297 (2017).
24. S. Tanaka *et al.*, Atomic-level models of the bacterial carboxysome shell. *Science* **319**, 1083–1086 (2008).
25. M. R. Yang *et al.*, Biogenesis of a bacterial metabolosome for propanediol utilization. *Nat. Commun.* **13**, 2920 (2022).
26. R. Q. Zhou *et al.*, Structure and assembly of the α-carboxysome in the marine cyanobacterium. *Nat. Plants* **10**, 661–672 (2024).
27. F. Cai *et al.*, The structure of CcmP, a tandem bacterial microcompartment domain protein from the beta-carboxysome, forms a subcompartment within a microcompartment. *J. Biol. Chem.* **288**, 16055–16063 (2013).
28. M. G. Klein *et al.*, Identification and structural analysis of a novel carboxysome shell protein with implications for metabolite transport. *J. Mol. Biol.* **392**, 319–333 (2009).
29. A. M. Larsson, D. Hasse, K. Valegard, I. Andersson, Crystal structures of beta-carboxysome shell protein CcmP: Ligand binding correlates with the closed or open central pore. *J. Exp. Bot.* **68**, 3857–3867 (2017).
30. Y. Q. Sun *et al.*, Decoding the absolute stoichiometric composition and structural plasticity of α-carboxysomes. *mBio* **13**, e03629-21 (2022).
31. O. Erbilgin, M. Sutter, C. A. Kerfeld, The structural basis of coenzyme A recycling in a bacterial organelle. *PLoS Biol.* **14**, e1002399 (2016).
32. J. B. Parsons *et al.*, Characterisation of PduS, the pdu metabolosome corrin reductase, and evidence of substructural organisation within the bacterial microcompartment. *PLoS One* **5**, e14009 (2010).
33. E. M. Sampson, C. L. V. Johnson, T. A. Bobik, Biochemical evidence that the pduS gene encodes a bifunctional cobalamin reductase. *Microbiol. (Reading)* **151**, 1169–1177 (2005).
34. S. Q. Cheng, T. A. Bobik, Characterization of the PduS cobalamin reductase of Salmonella enterica and its role in the Pdu microcompartment. *J. Bacteriol.* **192**, 5071–5080 (2010).
35. C. Aussignargues *et al.*, Structure and function of a bacterial microcompartment shell protein engineered to bind a [4Fe-4S] cluster. *J. Am. Chem. Soc.* **138**, 5262–5270 (2016).
36. M. Sutter, C. A. Kerfeld, B. M. C. Caller, a webtool to identify and analyze bacterial microcompartment types in sequence data. *Biol. Direct* **17**, 9 (2022).
37. S. Vitt, S. Prinz, M. Eisinger, U. Ermler, W. Buckel, Purification and structural characterization of the Na-translocating ferredoxin: NAD reductase (Rnf) complex of Clostridium tetanomorphum. *Nat. Commun.* **13**, 4209 (2022).
38. J. Gutiérrez-Fernández *et al.*, Key role of quinone in the mechanism of respiratory complex I. *Nat. Commun.* **11**, 4135 (2020).
39. M. Mirdita *et al.*, ColabFold: Making protein folding accessible to all. *Nat. Methods* **19**, 679–682 (2022).
40. J. Jumper *et al.*, Highly accurate protein structure prediction with AlphaFold. *Nature* **596**, 583–589 (2021).
41. J. Liu *et al.*, Enhancing alphafold-multimer-based protein complex structure prediction with MULTICOM in CASP15. *Commun. Biol.* **6**, 1140 (2023).
42. M. Yang *et al.*, Decoding the stoichiometric composition and organisation of bacterial metabolosomes. *Nat. Commun.* **11**, 1976 (2020).
43. L. G. Kristensen *et al.*, Hydroxyl radical mediated damage of proteins in low oxygen solution investigated using X-ray footprinting mass spectrometry. *J. Synchrotron Radiat.* **28**, 1333–1342 (2021).
44. X. J. Zheng, P. L. Wintrode, M. R. Chance, Complementary structural mass spectrometry techniques reveal local dynamics in functionally important regions of a metastable serpin. *Structure* **16**, 38–51 (2008).
45. A. Pang, M. J. Warren, R. W. Pickersgill, Structure of PduT, a trimeric bacterial microcompartment protein with a 4Fe-4S cluster-binding site. *Acta Crystallogr. Sect. D Struct. Biol.* **67**, 91–96 (2011).
46. C. Chowdhury, T. A. Bobik, Engineering the PduT shell protein to modify the permeability of the 1,2-propanediol microcompartment of Salmonella. *Microbiology (Reading)* **165**, 1355–1364 (2019).
47. M. Sommer *et al.*, Heterohexamers formed by CcmK3 and CcmK4 increase the complexity of beta carboxysome shells. *Plant Physiol.* **179**, 156 (2019).
48. M. Kuhns, D. Trifunovic, H. Huber, V. Müller, The Rnf complex is a Na coupled respiratory enzyme in a fermenting bacterium, Thermotoga maritima. *Commun. Biol.* **3**, 431 (2020).
49. M. P. Murphy, How mitochondria produce reactive oxygen species. *Biochem. J.* **417**, 1–13 (2009).
50. L. M. Utschig, U. Brahmachari, K. L. Mulfort, J. Niklas, O. G. Poluektov, Biohybrid photosynthetic charge accumulation detected by flavin semiquinone formation in ferredoxin-NADP+ reductase *Chem. Sci.* **13**, 6502–6511 (2022).
51. S. G. Mayhew, M. L. Ludwig, 2 flavodoxins and electron-transferring flavoproteins. *The Enzymes* **12**, 57–118 (1975).
52. S. L. J. Tan, J. M. Kan, R. D. Webster, Differences in proton-coupled electron-transfer reactions of flavin mononucleotide (FMN) and flavin adenine dinucleotide (FAD) between buffered and unbuffered aqueous solutions. *J. Phys. Chem. B* **117**, 13755–13766 (2013).
53. P. E. Mera, J. C. Escalante-Semerena, Dihydroflavin-driven adenosylation of 4-coordinate Co(II) corrinoids. *J. Biol. Chem.* **285**, 2911–2917 (2010).
54. S. Cheng, S. Sinha, C. Fan, Y. Liu, T. A. Bobik, Genetic analysis of the protein shell of the microcompartments involved in coenzyme B12-dependent 1,2-propanediol degradation by Salmonella. *J. Bacteriol.* **193**, 1385–1392 (2011).
55. J. S. Plegaria *et al.*, Structural and functional characterization of a short-chain flavodoxin associated with a noncanonical 1,2-propanediol utilization bacterial microcompartment. *Biochemistry* **56**, 5679–5690 (2017).
56. S. B. Mellor, K. Vavitsas, A. Z. Nielsen, P. E. Jensen, Photosynthetic fuel for heterologous enzymes: The role of electron carrier proteins. *Photosynth. Res.* **134**, 329–342 (2017).
57. A. F. V. Wagner, M. Frey, F. A. Neugebauer, W. Schafer, J. Knappe, The free-radical in pyruvate formate-lyase is located on glycine-734. *Proc. Natl. Acad. Sci. U.S.A.* **89**, 996–1000 (1992).
58. L. Kussmaul, J. Hirst, The mechanism of superoxide production by NADH:Ubiquinone oxidoreductase (complex I) from bovine heart mitochondria. *Proc. Natl. Acad. Sci. U.S.A.* **103**, 7607–7612 (2006).
59. D. A. Ravcheev, L. Moussu, S. Smajic, I. Thiele, Comparative genomic analysis reveals novel microcompartment-associated metabolic pathways in the human gut microbiome. *Front. Genet.* **10**, 636 (2019).

60. J. S. Plegaria, M. D. Yates, S. M. Glaven, C. A. Kerfeld, Redox characterization of electrode-immobilized bacterial microcompartment shell proteins engineered to bind metal centers. *ACS Appl. Bio Mater.* **3**, 685–692 (2020).
61. M. K. Akhtar, P. R. Jones, Deletion of iscR stimulates recombinant clostridial Fe-Fe hydrogenase activity and H-accumulation in BL21(DE3). *Appl. Microbiol. Biotechnol.* **78**, 853–862 (2008).
62. M. A. Larkin *et al.*, Clustal W and clustal X version 2.0. *Bioinformatics* **23**, 2947–2948 (2007).
63. S. Capella-Gutierrez, J. M. Silla-Martinez, T. Gabaldon, trimAl: A tool for automated alignment trimming in large-scale phylogenetic analyses. *Bioinformatics* **25**, 1972–1973 (2009).
64. A. M. Kozlov, D. Darriba, T. Flouri, B. Morel, A. Stamatakis, RAxML-NG: A fast, scalable and user-friendly tool for maximum likelihood phylogenetic inference. *Bioinformatics* **35**, 4453–4455 (2019).
65. R. Evans *et al.*, Protein complex prediction with AlphaFold-multimer. bioRxiv [Preprint] (2022). https://doi.org/10.1101/2021.10.04.463034 (Accessed 1 February 2024).
66. R. L. Gundry *et al.*, Preparation of proteins and peptides for mass spectrometry analysis in a bottom-up proteomics workflow. *Curr. Protoc. Mol. Biol.* **90**, 10.25.11–10.25.23 (2010).
67. M. Rosi *et al.*, An automated liquid jet for fluorescence dosimetry and microsecond radiolytic labeling of proteins. *Commun. Biol.* **5**, 866 (2022).
68. V. Fourmond, QSoas: A versatile software for data analysis. *Anal. Chem.* **88**, 5050–5052 (2016).
69. R. M. Mayall, V. I. Birss, S. E. Creager, Digital simulation and experimental validation of redox mediation at an electroactive monolayer-coated electrode. *J. Electrochem. Soc.* **167**, 046512 (2020).